Supporting Information

Nanotwin Engineering Enables Exceptional Thermal Stability in P-Type Bismuth Telluride Thermoelectrics

Chuandong Zhou[1,2], Jiaze Zhu[1,2], Shuxin Zhang[1], Zhen'ao Zhang[2], Zongwei Zhang[2], Jianfeng Cai[2], Qiang Zhang[2], Ruijie Li[2,4], Lianghan Fan[2], Jingtao Xu[3], Guoqiang Liu[2,4], Xiaojian Tan[2,4*], Bo Liang[1*], Jun Jiang[2,4*]

[1] *State Key Laboratory of Metastable Materials Science and Technology, Yanshan University, Qinhuangdao 066004, China*

[2] *Ningbo Institute of Materials Technology and Engineering, Chinese Academy of Sciences, Ningbo 315201, China*

[3] *Ningbo University of Technology, Ningbo 315211, China*

[4] *University of Chinese Academy of Sciences, Beijing 100049, China.*

E-mail: tanxiaojian@nimte.ac.cn; liangbo@ysu.edu.cn; jjun@nimte.ac.cn

Experimental Section

Samples Synthesis: To synthesize the Ag_9GaSe_6 and Ag_8SnSe_6 compounds, high-purity (5N) elemental Ag, Ga, and Se, or Ag, Sn, and Se were weighed in stoichiometric proportions and sealed in evacuated quartz tubes. The mixtures were melted at 1273 K for 4 hours and then quenched in cold water to obtain single-phase ingots of Ag_9GaSe_6 and Ag_8SnSe_6, respectively. For bulk thermoelectric samples, high-purity (5N) Bi, Sb, Cu, Te, along with the synthesized Ag_8SnSe_6 and Ag_9GaSe_6 compounds, were weighed according to the stoichiometric compositions of $Bi_{0.48}Sb_{1.52}Te_3 + x$ wt% Ag_8SnSe_6 ($x = 0.06$, 0.08, 0.1), $Bi_{0.48}Sb_{1.52}Te_3 + x$ wt% Ag_9GaSe_6 ($x = 0.05$, 0.06, 0.07, 0.08) and $Bi_{0.48}Sb_{1.52-y}Cu_yTe_3 + 0.06$ wt% Ag_9GaSe_6 ($y = 0.002$, 0.003, 0.004, 0.005). The mixtures were sealed into evacuated quartz tubes (Φ10 mm), heated to 1023 K for 1 hour, then gently rocked for 1 hour to ensure homogeneity, and finally quenched in water to obtain solidified ingots. The resulting ingots were ground into fine powders and were then loaded into Φ20 mm graphite dies and consolidated by spark plasma sintering (SPS) at 693 K under a uniaxial pressure of 60 MPa for 10 minutes to form dense bulk samples.

Thermoelectric Properties Measurement: The HD sample was cut into long strips with dimensions of 3 mm × 3 mm × 10 mm using an electric spark cutting machine. The Seebeck coefficient and electrical conductivity were measured simultaneously using a four-probe method in a low-pressure argon environment with the ZEM-3 system. The zone-melted sample was cut into thin slices with dimensions of 12.7 mm × 1.8 mm. The thermal diffusivity (D) was measured using the LFA-467 laser flash instrument, the density was determined using the Archimedes method, and the total thermal conductivity was calculated using the specific heat capacity obtained by the Dulong-Petit limit for Cp. The room temperature Hall coefficient (R_H) was measured using a comprehensive physical property measurement system (PPMS-9 Evercool). The Hall carrier concentration (n_H) and mobility (μ_H) were calculated using the equations $n_H = 1/(eR_H)$ and $\mu_H = \sigma R_H$, respectively.

Mechanical Performance Characterization: The Vickers hardness of each sample

was measured three times using a microhardness tester (HV-1000) under a load of 50 N applied for 10 s. The compressive strength (σ_{bc}) was evaluated using a universal testing machine (Zwick/Roell Z030) with bar-shaped specimens of dimensions $5 \times 4.5 \times 17$ mm³ and a loading rate of 0.5 mm min^{-1}. The compressive strength was calculated as $\sigma_{bc} = F_{bc}/\mathrm{A}$, where F_{bc} is the maximum load before failure, and A is the cross-sectional area of the specimen.

Structure Characterization: The in-plane phase structure of the bulk samples was analyzed using X-ray diffraction (XRD). The microstructure was examined with a scanning electron microscope (SEM) and high-resolution transmission electron microscope (HRTEM), and the elemental distribution was analyzed using energy-dispersive X-ray spectroscopy (EDS). Electron backscatter diffraction (EBSD) measurements were performed using a field-emission scanning electron microscope (FE-SEM) equipped with an Oxford Symmetry EBSD detector. Prior to data acquisition, the sample surfaces were carefully polished and subsequently treated by ion milling to obtain a strain-free surface suitable for EBSD analysis. Measurements were carried out at an accelerating voltage of 20 kV, a working distance of ~15 mm, and a step size of 0.1–0.3 μm depending on the microstructural features.

TE Module Fabrication and Measurement: The TE device measures 20 mm × 20 mm and consists of 17 pairs of *p*-*n* legs. The preparation process for the bismuth telluride-based TE device is shown in Supporting Information Figure S22. The *p*-type legs are composed of $Bi_{0.48}Sb_{1.516}Cu_{0.004}Te_3$ + 0.06 wt% Ag_9GaSe_6 samples, while the *n*-type legs are made of zone-melted $Bi_2Te_{2.7}Se_{0.3}$, with their thermoelectric performance detailed in the supporting information S23. Both *p*-type and *n*-type legs are plated with Ni as a diffusion barrier layer and then cut into particles of 5mm × 2.3mm × 2.3mm (*p*-type) and 5mm × 2.3mm × 2.07mm (*n*-type). The *p*- and *n*-legs are alternately soldered on an alumina plate with copper electrodes. The device was tested using a custom-built testing system, and the conversion efficiency η was calculated using the formula $\eta = P/(Q_c + P)$, where P is the measured output power and Q_c is the measured heat flow at the cold end.

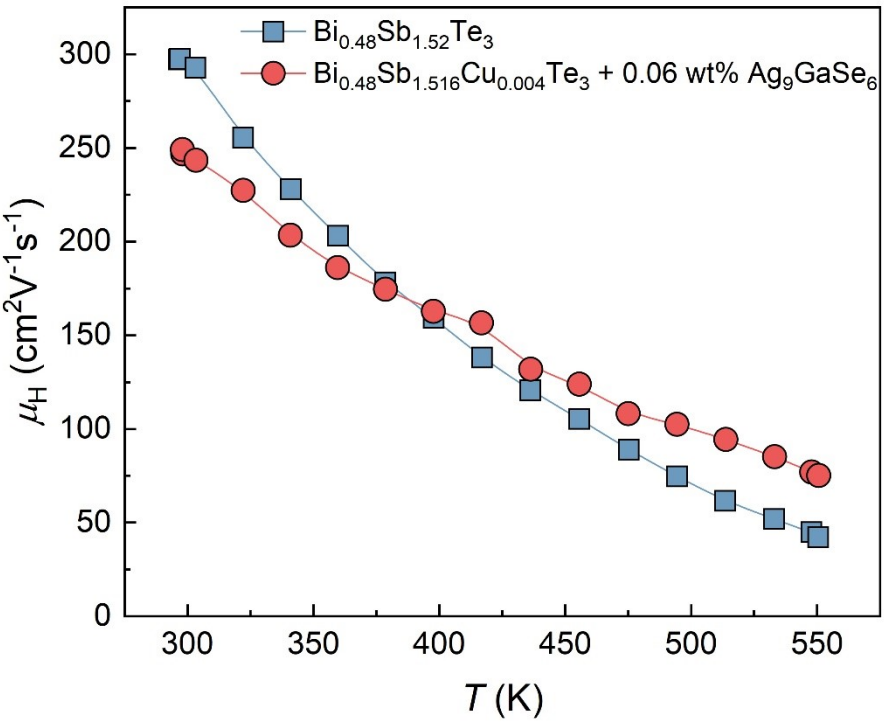

Fig. S1. Temperature-dependent Hall mobility (μ_H) for $(Bi,Sb)_2Te_3$ samples with and without nanotwins measured over 300-550 K.

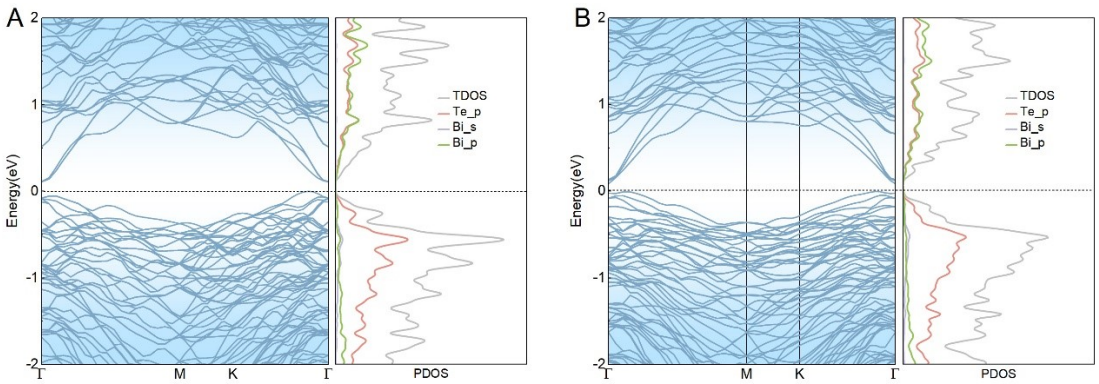

Fig. S2. Calculated electronic band structure and projected density of states (PDOSs) of $(Bi,Sb)_2Te_3$ supercells (left) without and (right) with nanotwin according to density functional theory (DFT) simulations.

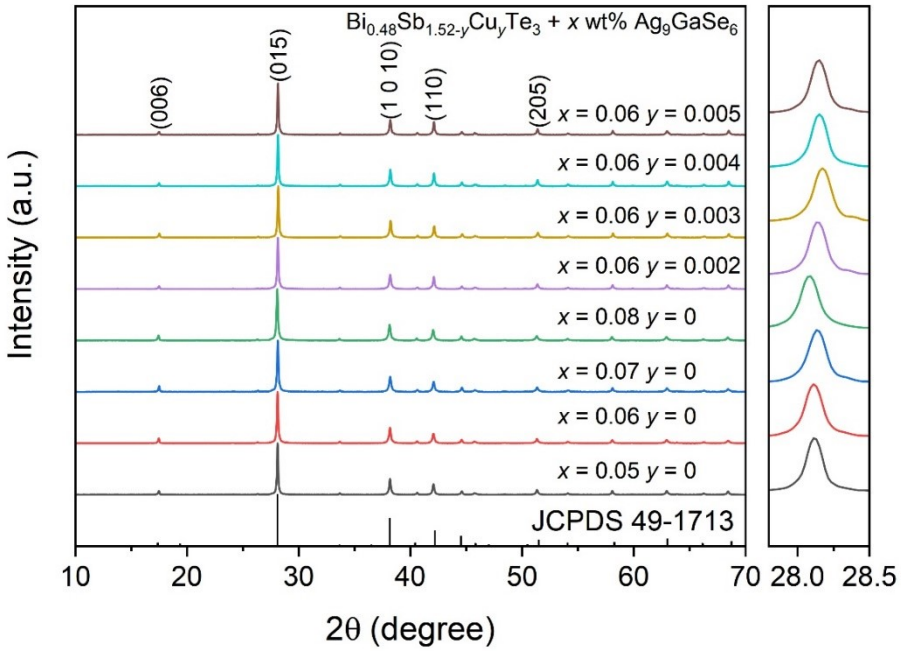

Fig. S3. XRD patterns of $Bi_{0.48}Sb_{1.52-y}Cu_yTe_3$ + *x* wt% Ag_9GaSe_6 samples.

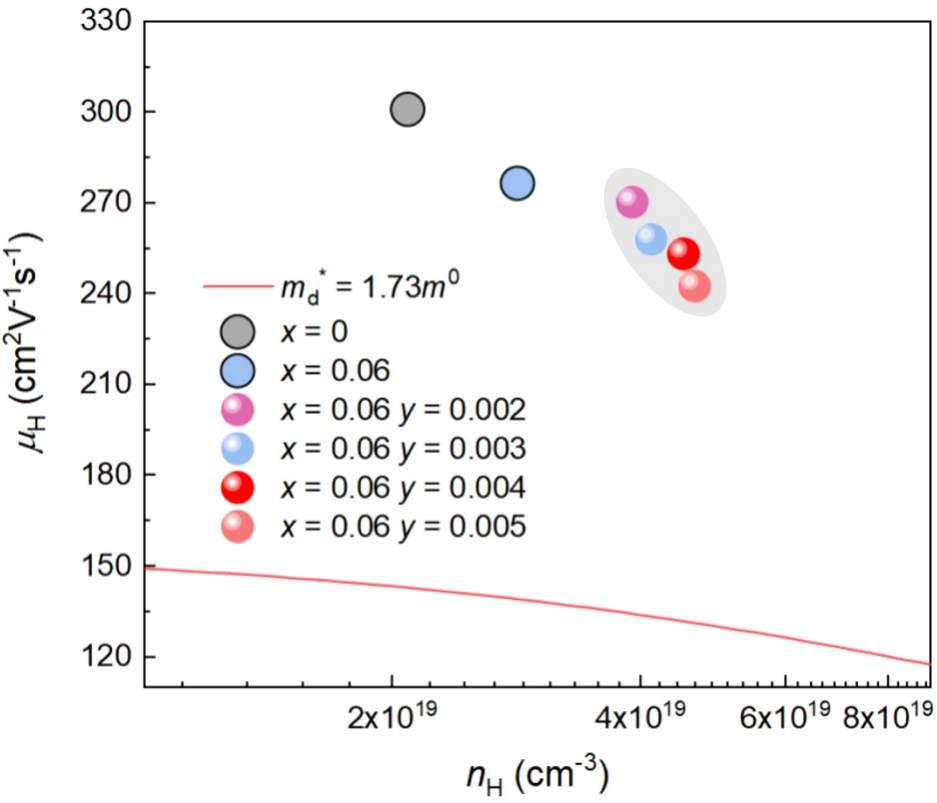

Fig. S4. Carrier mobility μ_H as a function of carrier concentration n_H.

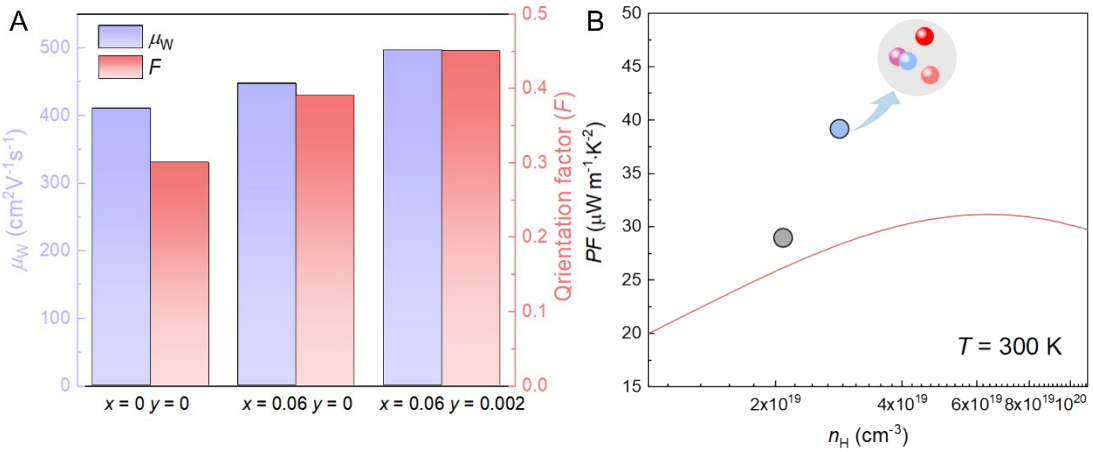

Fig. S5. (A) Weighted mobility μ_W and orientation factor F of selected samples. (B) Power factor *PF* as a function of carrier concentration n_H at 300 K, with the theoretical trend shown for comparison.

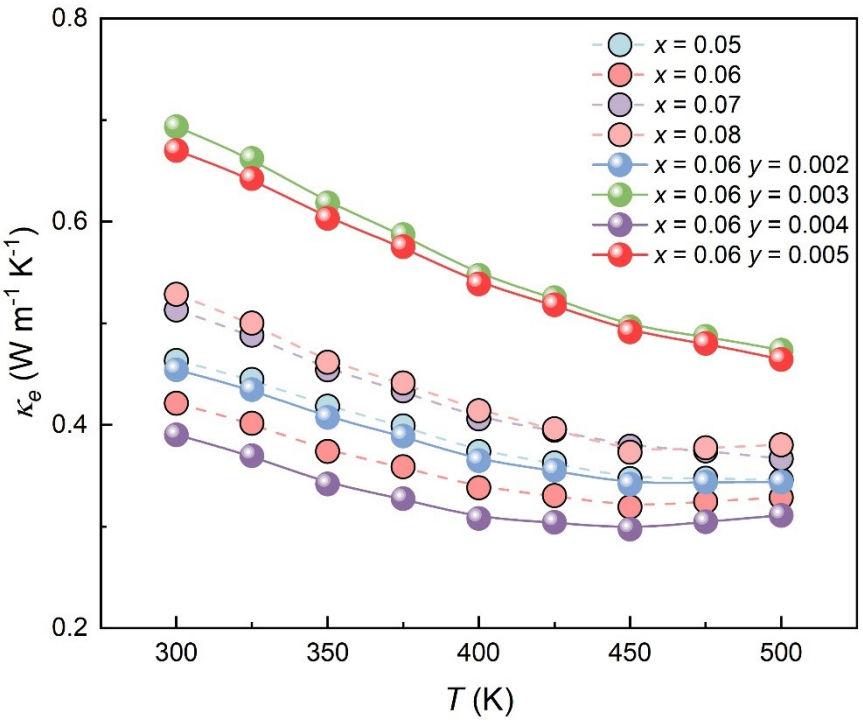

Fig. S6. Temperature dependence of the electronic thermal conductivity κ_e for $Bi_{0.48}Sb_{1.52-y}Cu_yTe_3$ + x wt% Ag_9GaSe_6 samples with varying compositions.

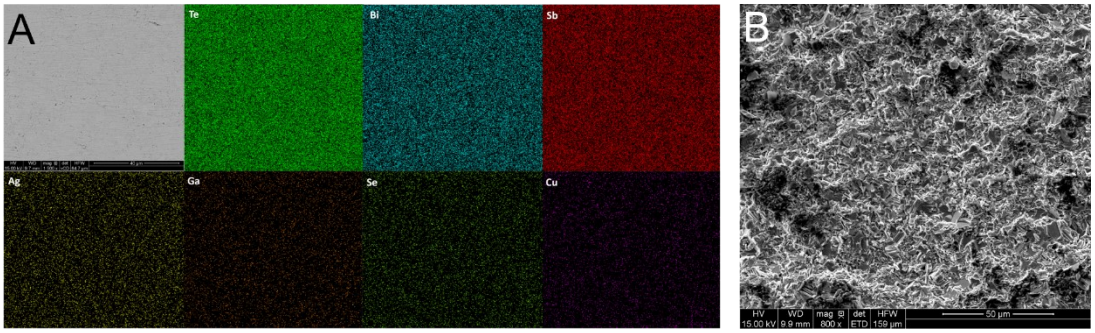

Fig. S7. (A) SEM image and corresponding elemental maps of the polished surface of the $Bi_{0.48}Sb_{1.516}Cu_{0.004}Te_3$ + 0.06 wt% Ag_9GaSe_6 sample. (B) Cross-sectional SEM image of the $Bi_{0.48}Sb_{1.516}Cu_{0.004}Te_3$ + 0.06 wt% Ag_9GaSe_6 sample.

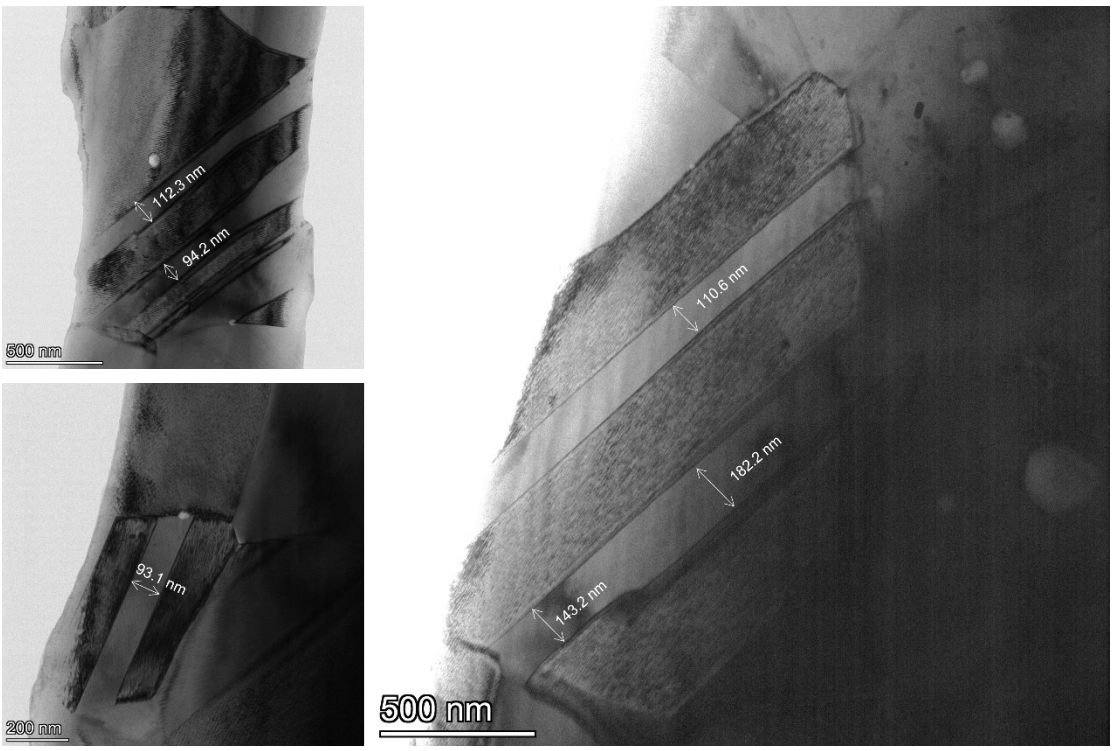

Fig. S8. TEM images reveal the presence of numerous nanoscale twin structures within the sample, with twin thickness ranging from approximately 90 to 180 nm.

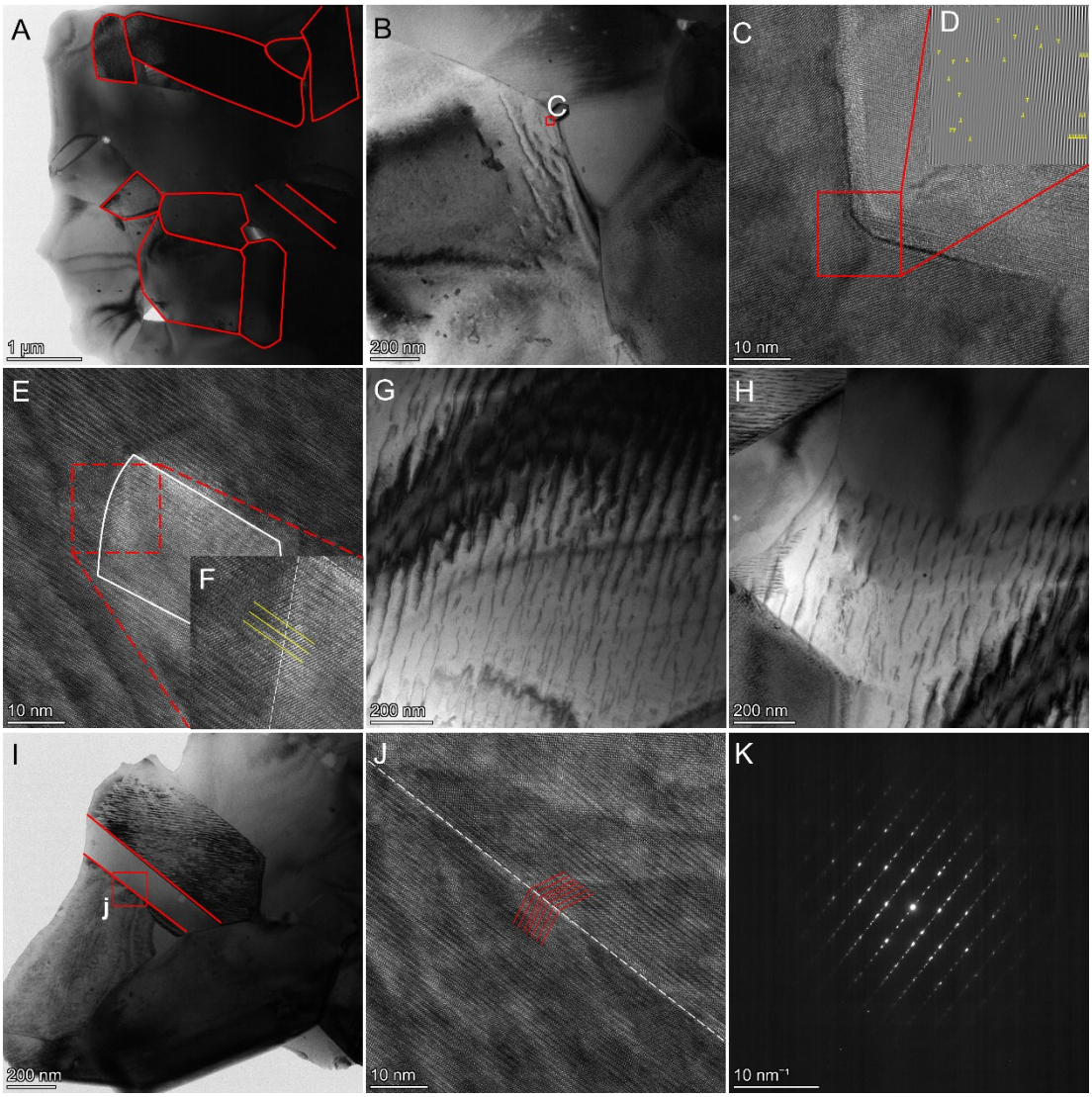

Fig. S9. (A) Dark-field TEM image showing the microstructure of the sample. (B) Nanoscale precipitates are observed at the grain boundary. (C–F) High-resolution images of the interface between precipitates and matrix, with (D) showing a magnified inset. (G, H) Dark-field images reveal dense dislocation arrays. (I) Twin structure with corresponding high-resolution image (J) and selected area electron diffraction SAED pattern (K).

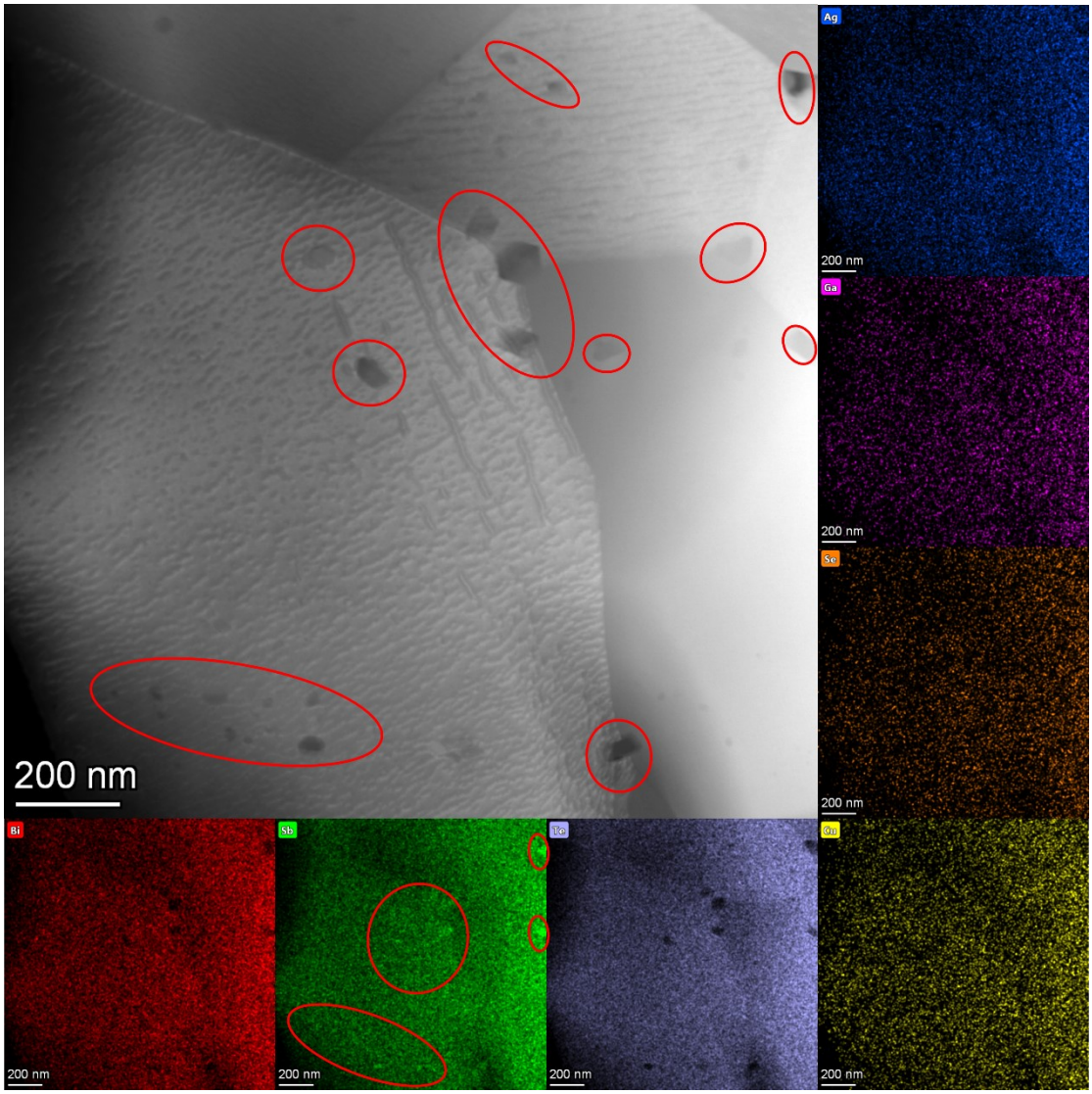

Fig. S10. TEM image and corresponding EDS elemental mapping.

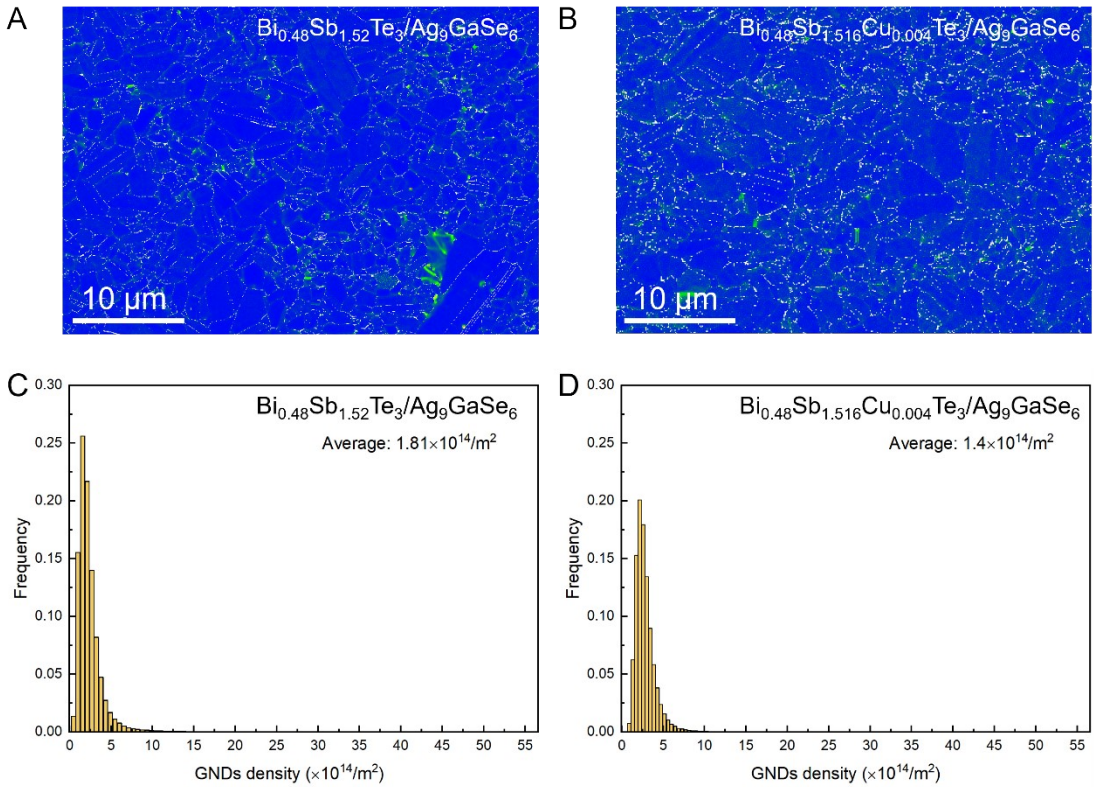

Fig. S11. EBSD-derived geometrically necessary dislocation (GND) density in AGS and AGS/Cu samples. (A, B) GND density maps of $Bi_{0.48}Sb_{1.52}Te_3/Ag_9GaSe_6$ (AGS) and $Bi_{0.48}Sb_{1.516}Cu_{0.004}Te_3/Ag_9GaSe_6$ (AGS/Cu), respectively. (C, D) Statistical distributions of GND density for AGS and AGS/Cu, respectively.

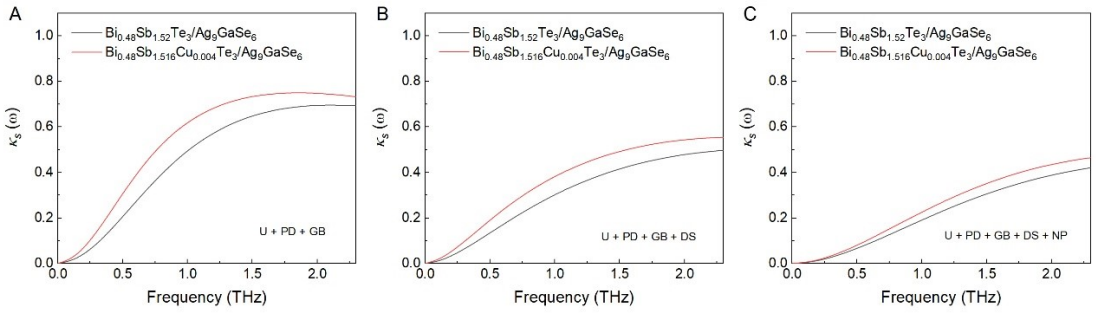

Fig. S12. Comparison of frequency-dependent spectral lattice thermal conductivity $\kappa_s(\omega)$ between AGS and AGS/Cu samples without considering nanotwin scattering, calculated using the Debye-Callaway model. (A) $\kappa_s(\omega)$ including Umklapp + point-defect + grain-boundary (U + PD + GB) scattering. (B) $\kappa_s(\omega)$ including U + PD + GB + dislocation (DS) scattering. (C) $\kappa_s(\omega)$ including U + PD + GB + DS + nanoprecipitate (NP) scattering.

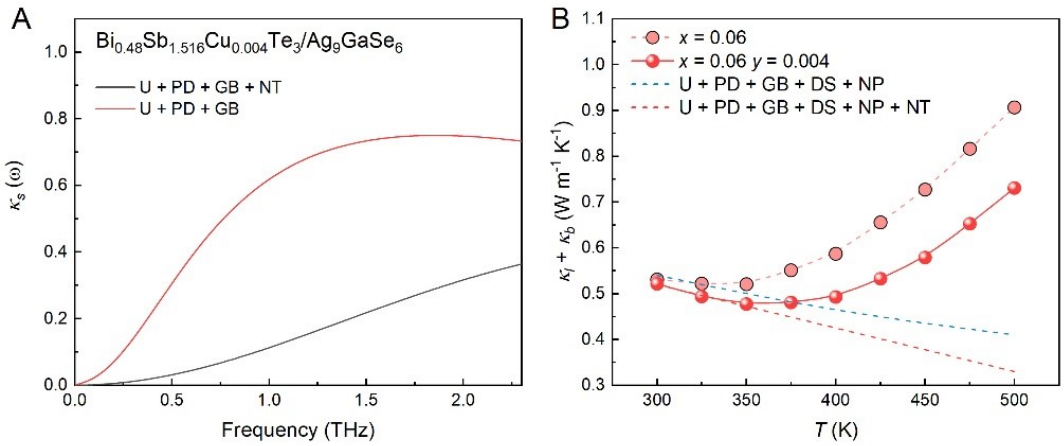

Fig. S13. (A) Effect of nanotwin scattering on the spectral lattice thermal conductivity $\kappa_s(\omega)$ of the $Bi_{0.48}Sb_{1.516}Cu_{0.004}Te_3/Ag_9GaSe_6$ (AGS/Cu) sample. The red curve shows $\kappa_s(\omega)$ including U + PD + GB scattering, while the black curve further incorporates nanotwin (NT) scattering (U + PD + GB + NT), leading to a pronounced suppression of $\kappa_s(\omega)$, especially in the mid-frequency region. (B) Temperature-dependent total thermal conductivity ($\kappa_l + \kappa_b$) of the AGS ($x = 0.06$) and nanotwinned AGS/Cu ($x = 0.06$, $y = 0.004$) samples.

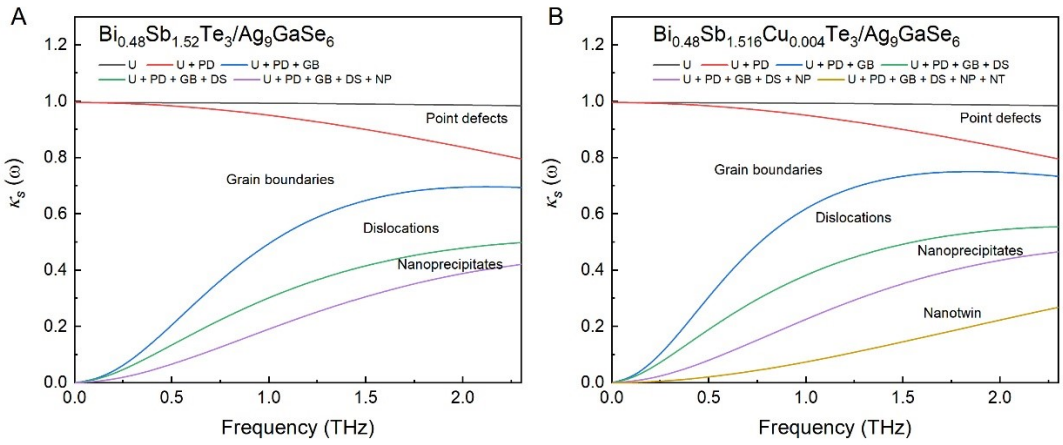

Fig. S14. Decomposition of phonon-scattering contributions to the spectral lattice thermal conductivity $\kappa_s(\omega)$ in (A) AGS and (B) AGS/Cu samples, calculated using the Debye-Callaway model.

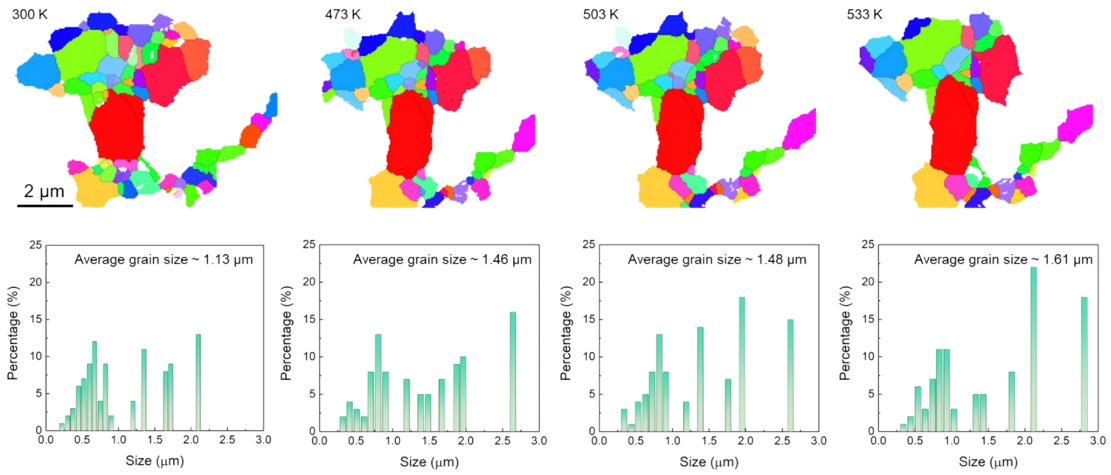

Fig. S15. Electron backscatter diffraction (EBSD) inverse pole figure (IPF) maps and corresponding grain size distributions of the ordinary grain subset at different annealing temperatures.

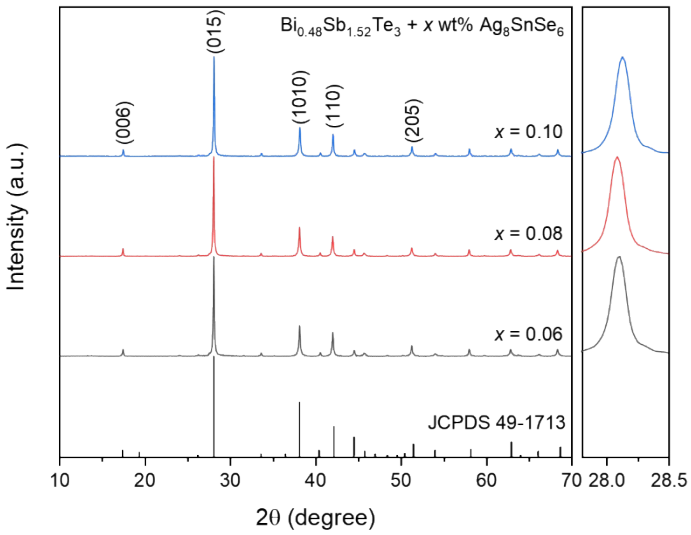

Fig. S16. XRD patterns of $Bi_{0.48}Sb_{1.52-y}Cu_yTe_3$ + *x* wt% Ag_8SnSe_6 samples.

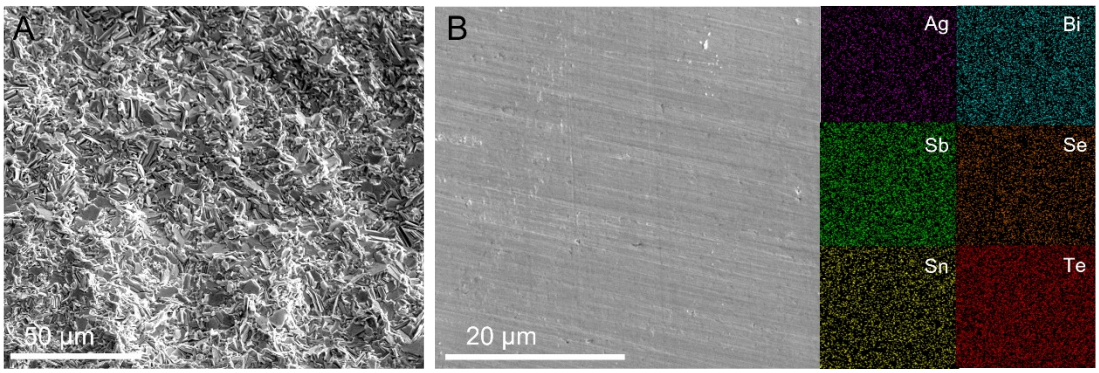

Fig. S17. (A) Cross-sectional SEM image of the $Bi_{0.48}Sb_{1.52}Te_3$ + 0.08 wt% Ag_8SnSe_6 sample. (B) SEM image and corresponding elemental maps of the polished surface of the $Bi_{0.48}Sb_{1.52}Te_3$ + 0.08 wt% Ag_8SnSe_6 sample.

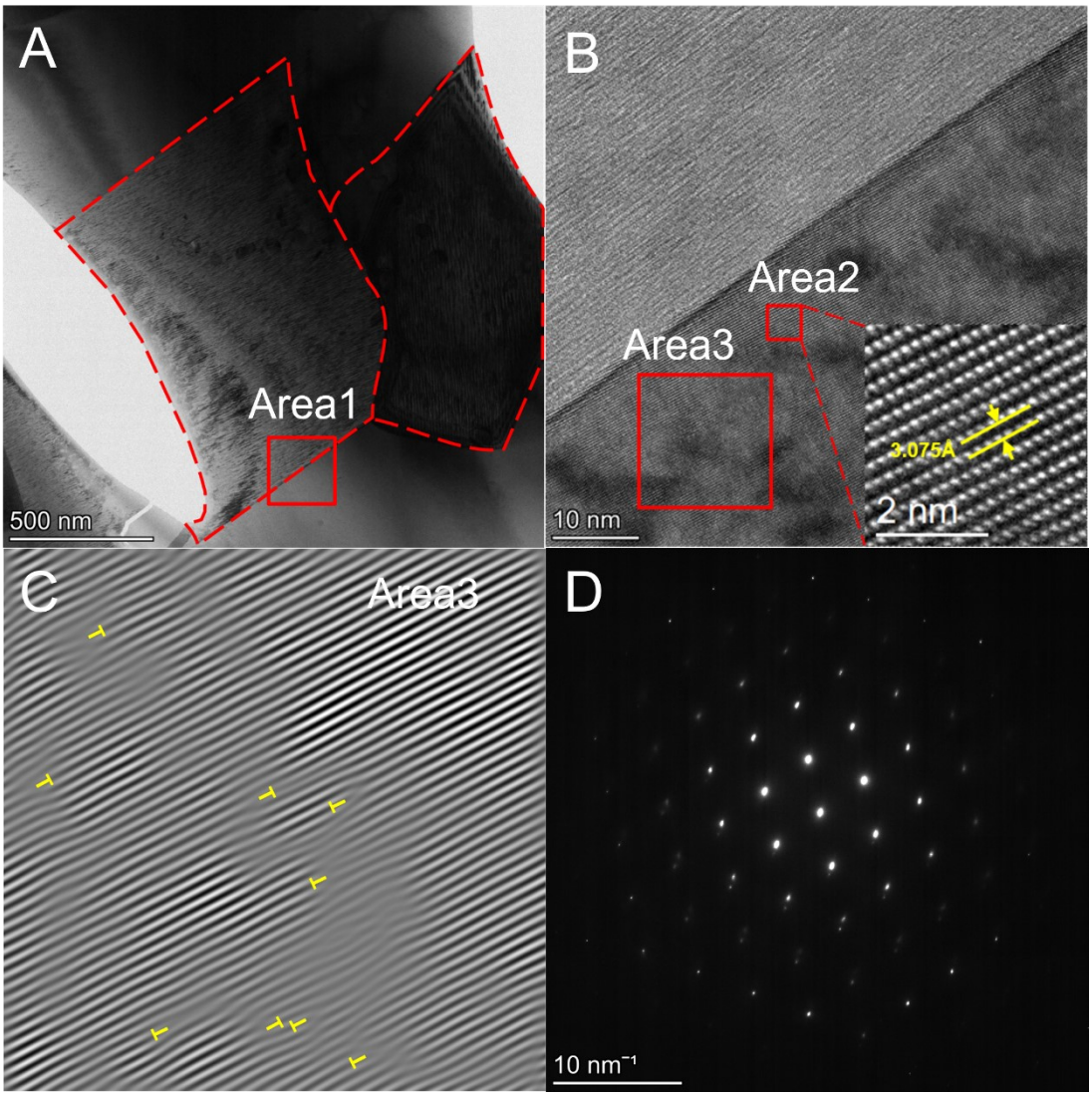

Fig. S18. (A) TEM dark-field image of the $Bi_{0.48}Sb_{1.52}Te_3$ + 0.08 wt% Ag_8SnSe_6 sample. (B) High-resolution TEM image of Area1 from (A), with the inset showing the atomic-resolution structure of Area2. (C) Inverse fast Fourier transform IFFT image of Area3 from (B), where yellow "T" symbols indicate dislocation sites. (D) Selected area electron diffraction SAED pattern corresponding to Area3.

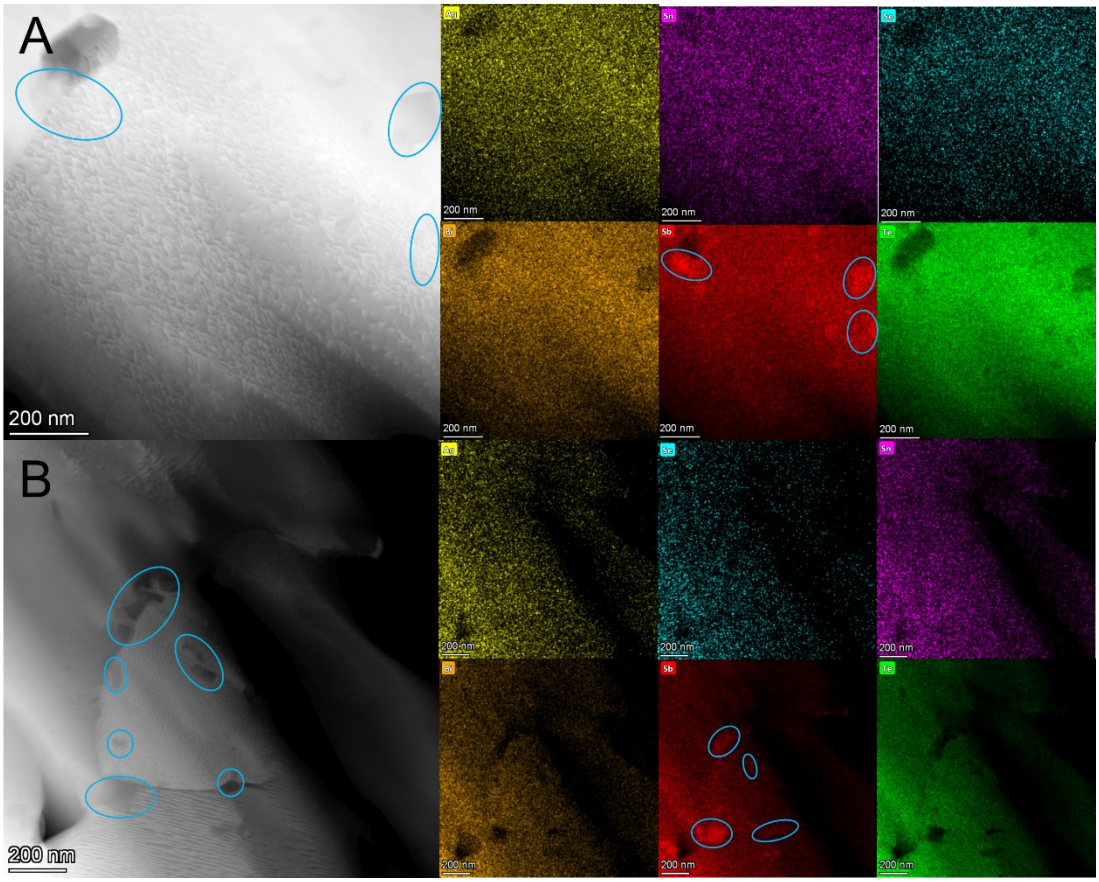

Fig. S19. (A) TEM image of the $Bi_{0.48}Sb_{1.52}Te_3$ + 0.08 wt% Ag_8SnSe_6 sample showing nanoscale precipitates and corresponding elemental mapping. (B) TEM image and elemental distribution at grain boundaries. Blue ellipses indicate the regions of precipitates or elemental enrichment.

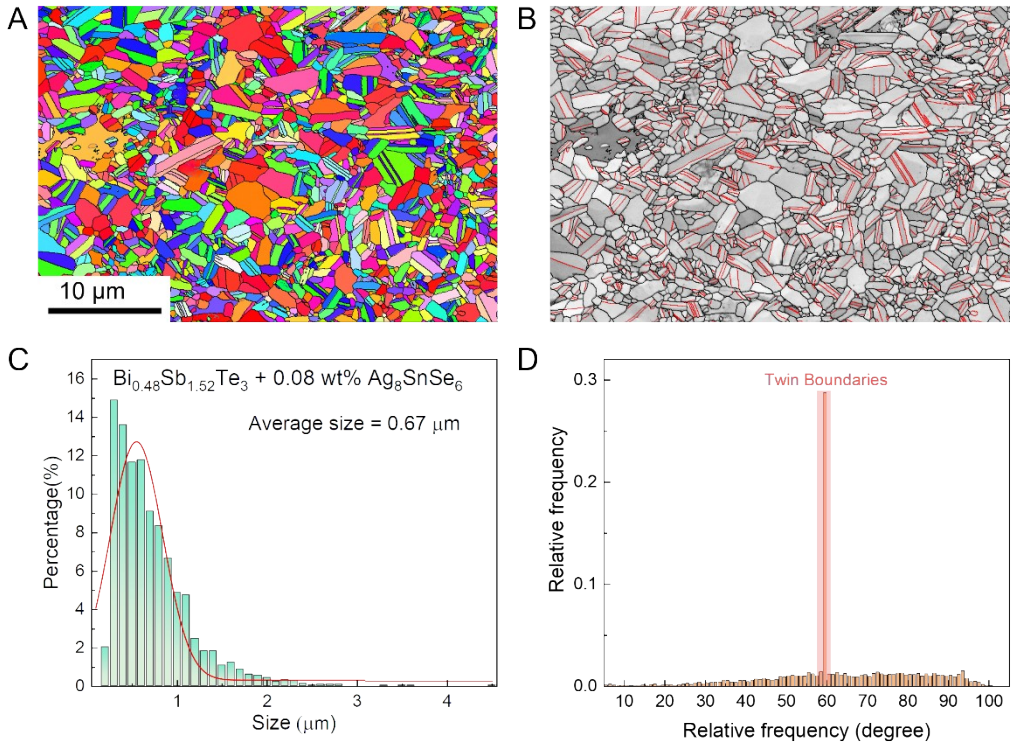

Fig. S20. (A) EBSD maps and statistical analysis of the $Bi_{0.48}Sb_{1.52}Te_3$ + 0.08 wt% Ag_8SnSe_6 sample before annealing. (B) Twin boundaries (red lines) are densely distributed between grains. The (C) grain size and (D) grain boundary angle distribution histogram confirms a high twin fraction and refined grain structure.

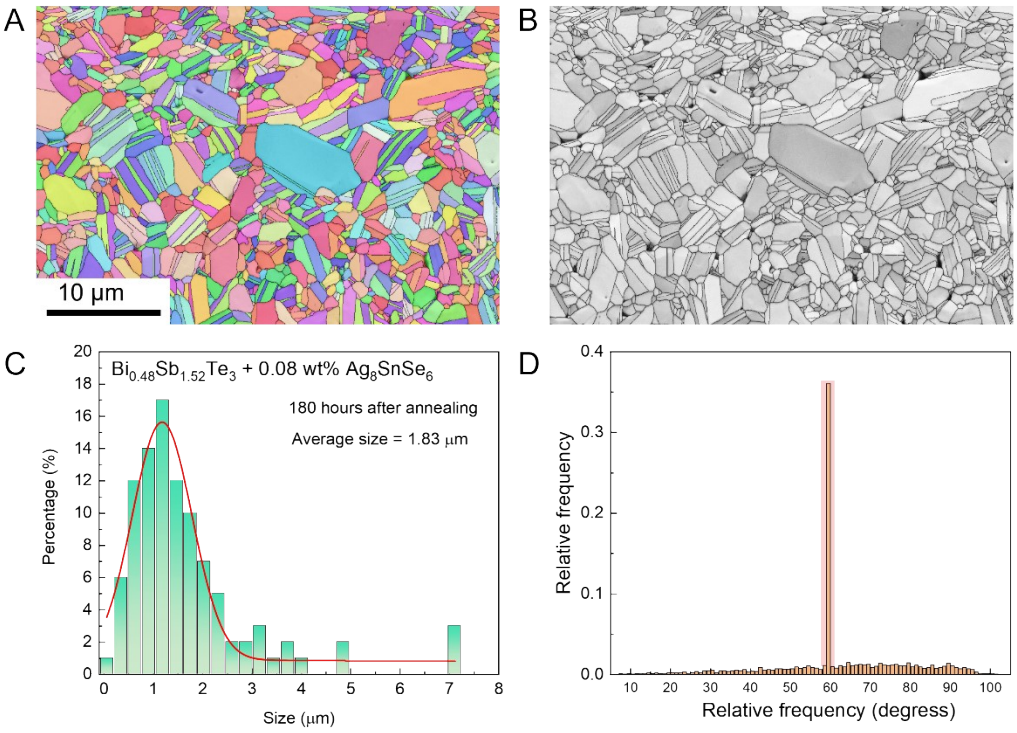

Fig. S21. (A) EBSD map of the $Bi_{0.48}Sb_{1.52}Te_3$ + 0.08 wt% Ag_8SnSe_6 sample after annealing at 533 K for 180 h; (B) corresponding grain boundary image; (C) grain size distribution with an average size of 1.83 μm; (D) misorientation angle distribution.

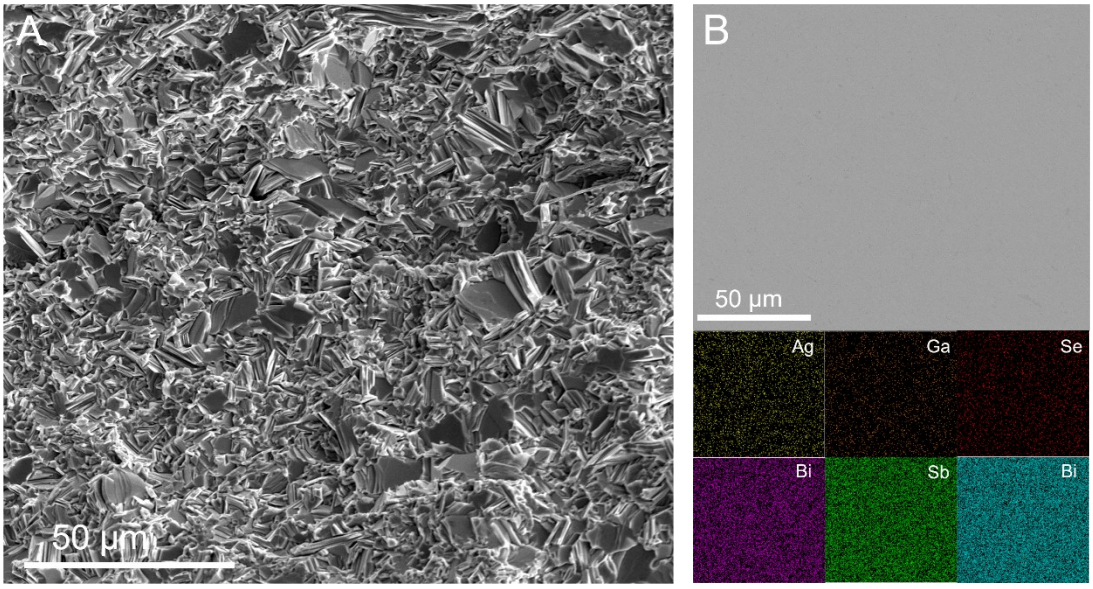

Fig. S22. (A) Cross-sectional SEM image of the $Bi_{0.48}Sb_{1.52}Te_3$ + 0.06 wt% Ag_9GaSe_6 sample. (B) SEM image and corresponding elemental maps of the polished surface of the $Bi_{0.48}Sb_{1.52}Te_3$ + 0.06 wt% Ag_9GaSe_6 sample.

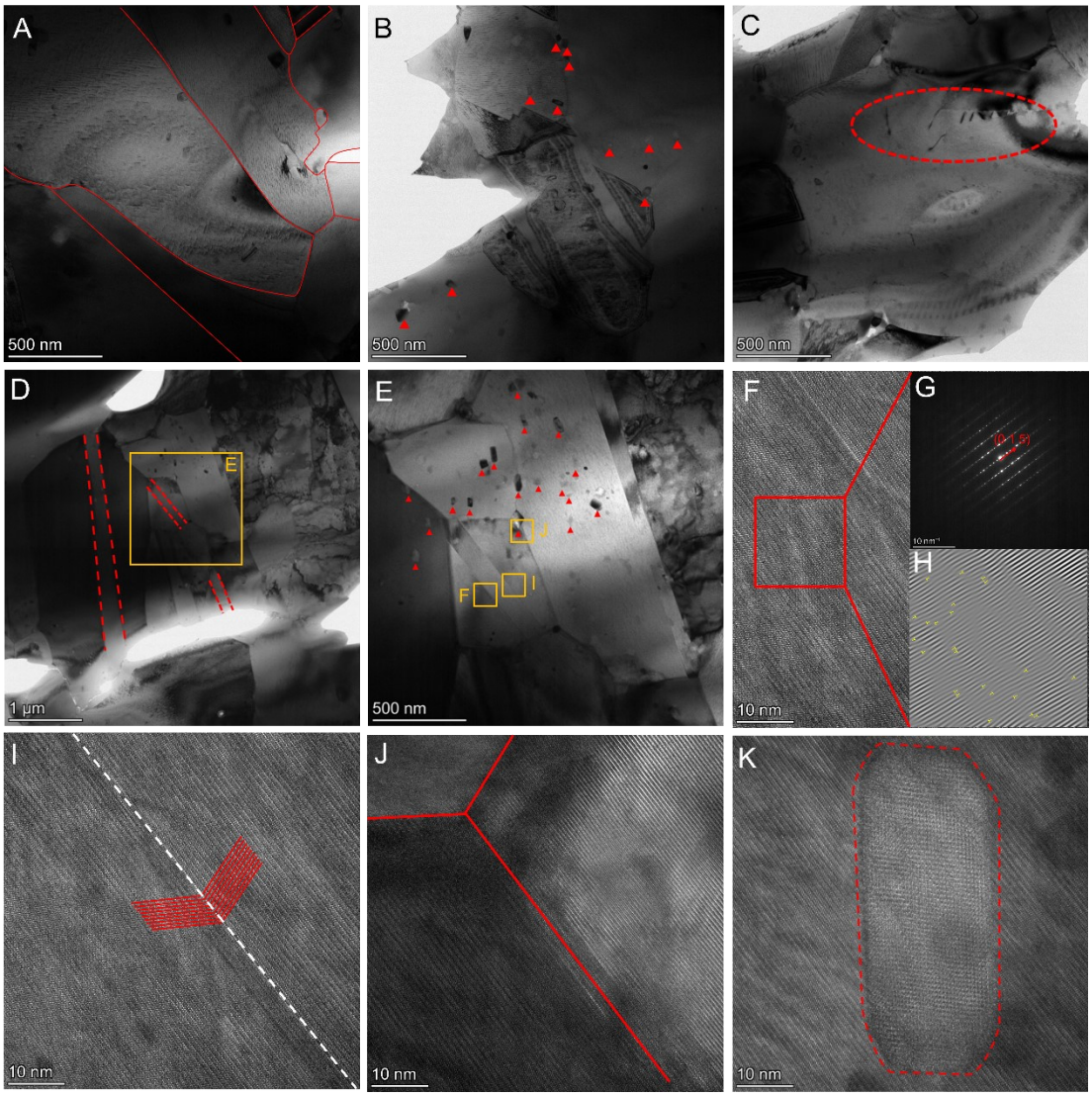

Fig. S23. (A) TEM image of the $Bi_{0.48}Sb_{1.52}Te_3$ + 0.06 wt% Ag_9GaSe_6 sample showing distinct grain boundaries; (B) nanoscale precipitates marked by red arrows; (C) dense dislocations observed in the local region; (D) typical twin structure identified; (E) magnified image of D highlighting twins and nanoscale precipitates; (F) high-resolution image of the twin region; (G) corresponding selected area electron diffraction (SAED) pattern; (H) inverse fast Fourier transform (IFFT) image; (I) identified twin boundary; (J) high-resolution image showing a grain boundary; (K) HRTEM image of a nanoscale precipitate.

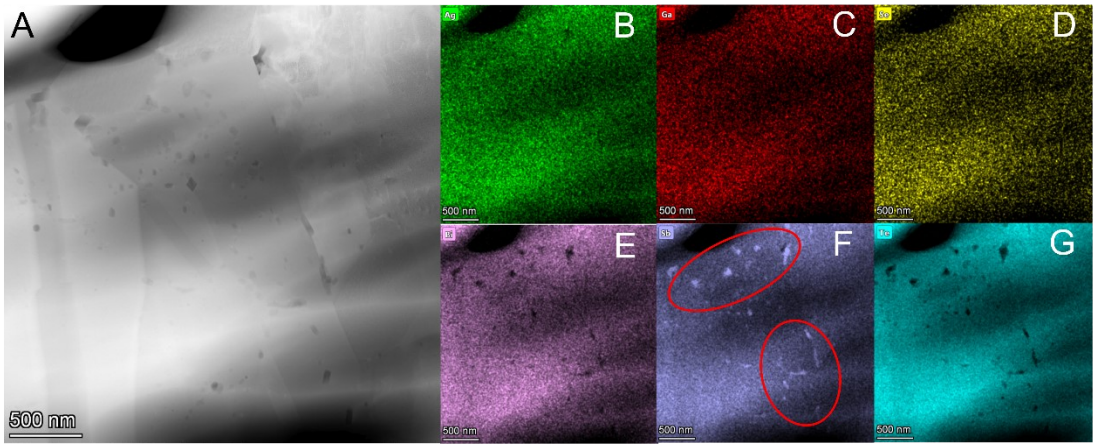

Fig. S24. (A) TEM image of the $Bi_{0.48}Sb_{1.52}Te_3$ + 0.06 wt% Ag_9GaSe_6 sample; (B–G) corresponding elemental mappings of Ag, Ga, Sn, Te, Sb, and Se, respectively. Several enriched regions indicate the presence of precipitates.

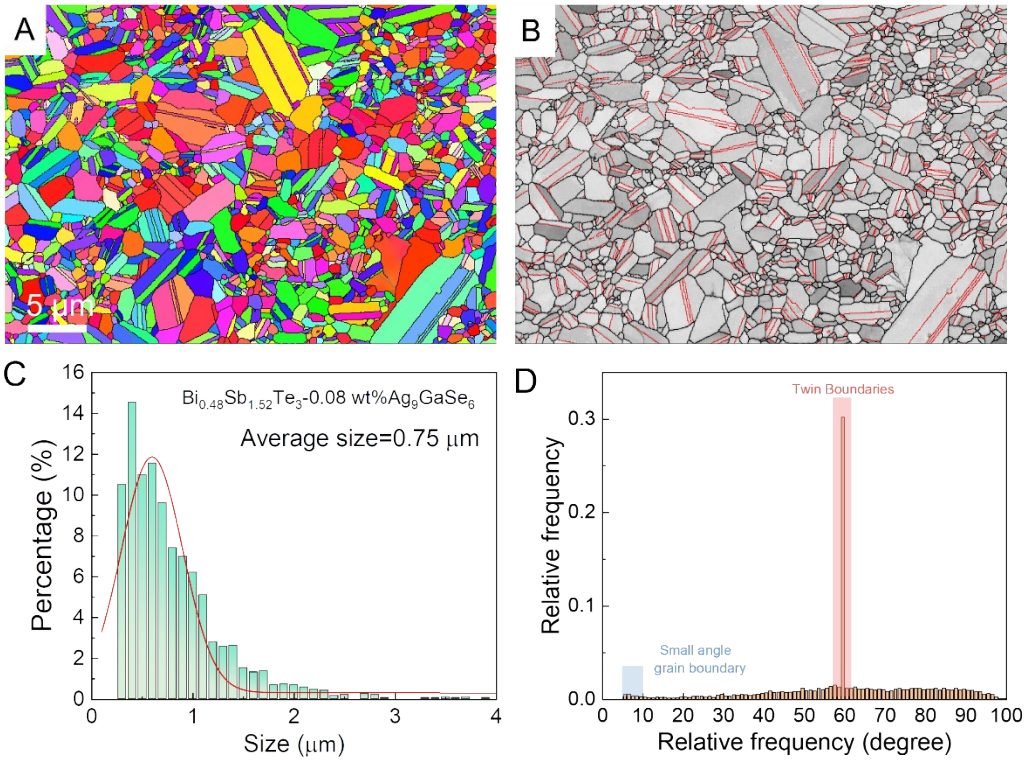

Fig. S25. (A) EBSD maps and statistical analysis of the $Bi_{0.48}Sb_{1.52}Te_3$ + 0.06 wt% Ag_9GaSe_6 sample before annealing. (B) Twin boundaries (red lines) are densely distributed between grains. The (C) grain size and (D) grain boundary angle distribution histogram confirms a high twin fraction and refined grain structure.

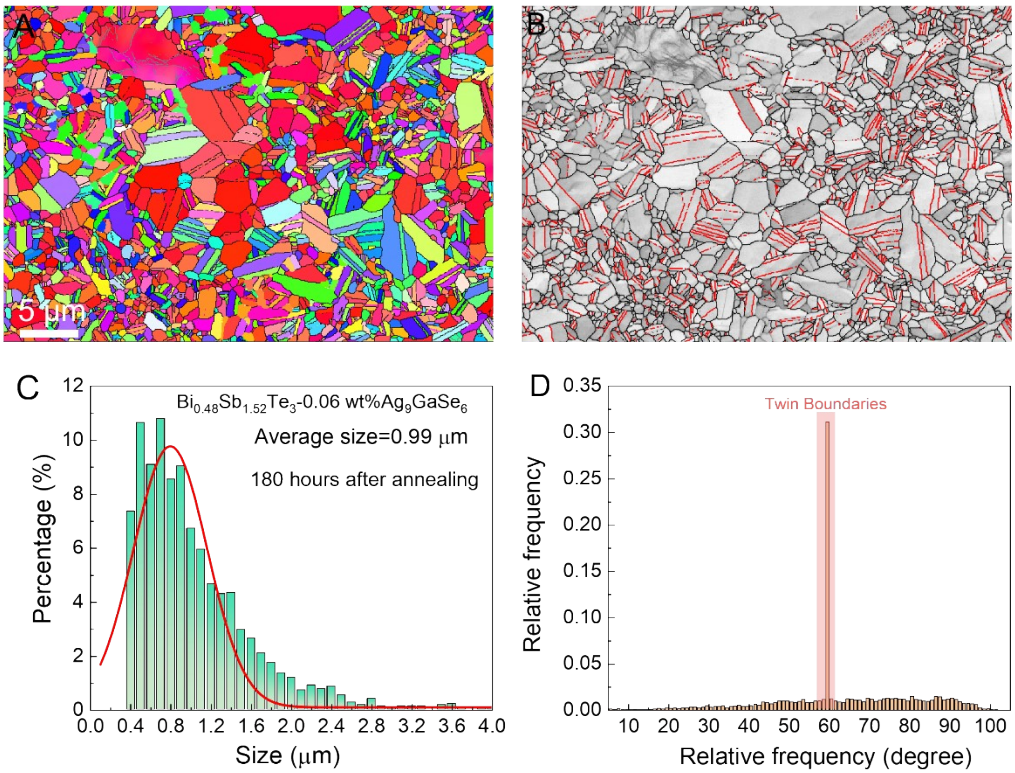

Fig. S26. (A) EBSD map of the $Bi_{0.48}Sb_{1.52}Te_3$ + 0.06 wt% Ag_9GaSe_6 sample after annealing at 533 K for 180 h; (B) corresponding grain boundary image; (C) grain size distribution with an average size of 0.99 μm; (D) misorientation angle distribution.

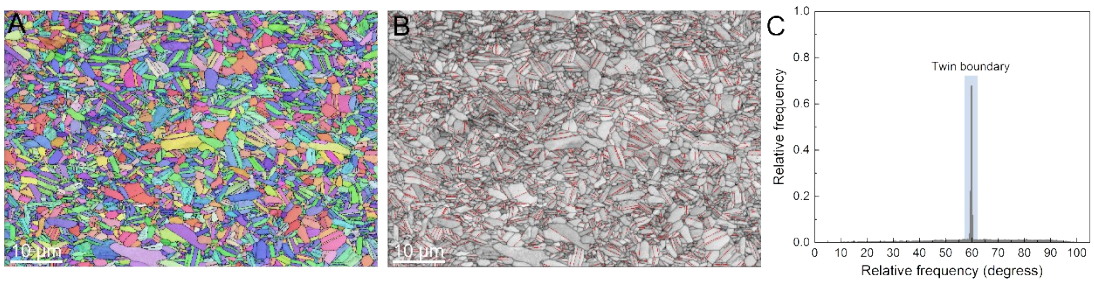

Fig. S27. (A) Corresponding grain boundary misorientation distribution demonstrating predominant twin-related angles; (B) Orientation map showing dense twin boundary networks; (C) Statistical analysis confirming high twin boundary density (>70%).

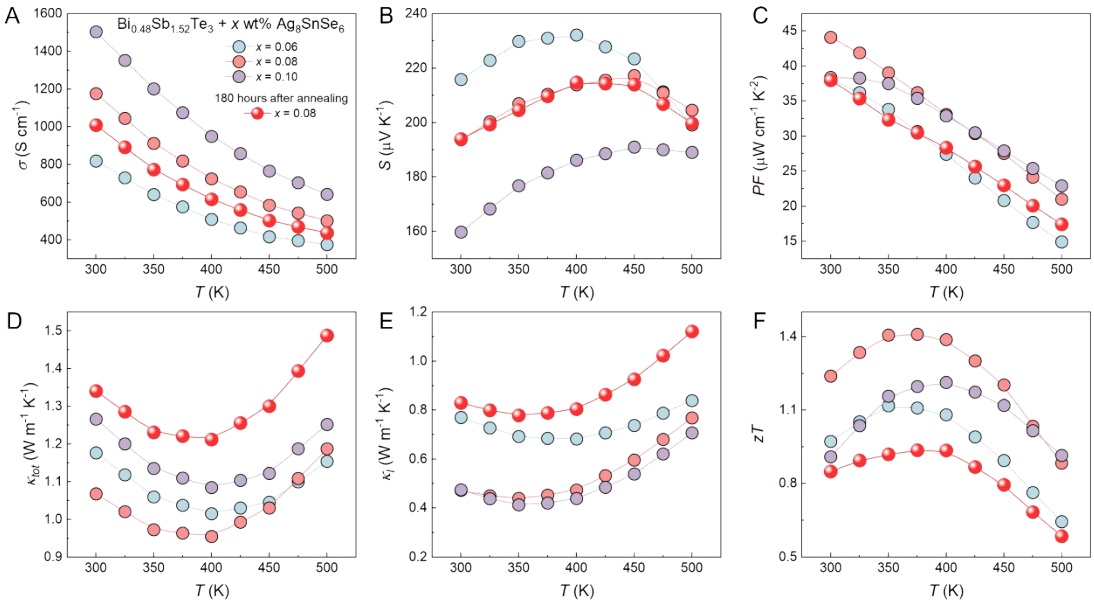

Fig. S28. Thermoelectric properties of the ASS series samples: (A) electrical conductivity, (B) Seebeck coefficient, (C) power factor, (D) lattice thermal conductivity, (E) total thermal conductivity, and (F) zT values as a function of temperature.

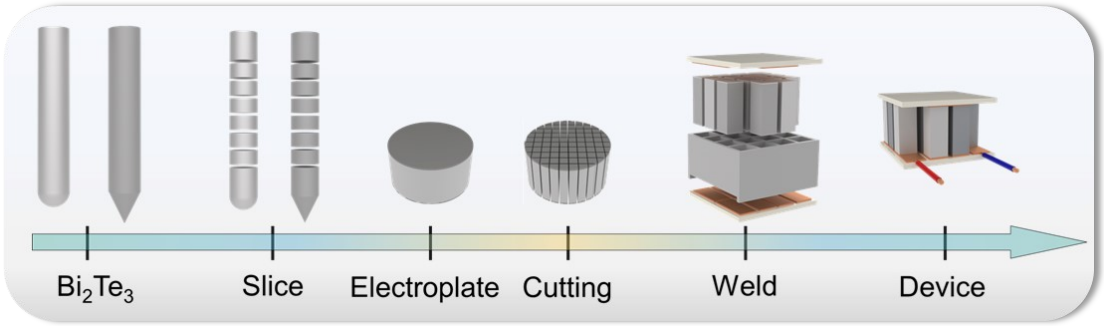

Fig. S29. The schematic diagram illustrates the fabrication flow of the TE modules in this work.

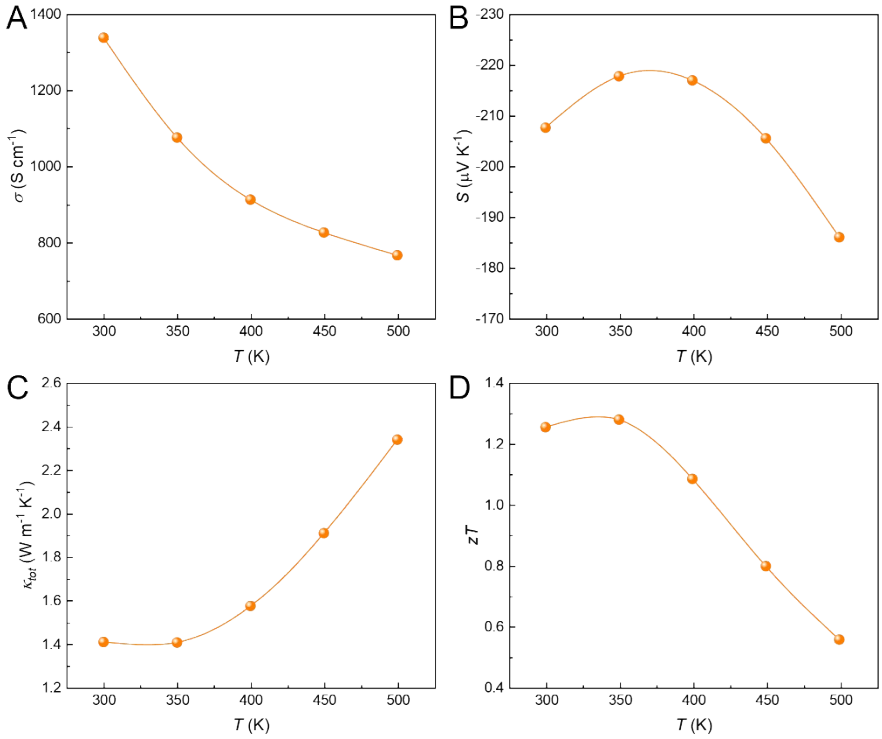

Fig. S30. Thermoelectric properties of zone-melted *n*-type Bi_2Te_3: (A) electrical conductivity, (B) Seebeck coefficient, (C) total thermal conductivity, and (D) *zT* values as a function of temperature.

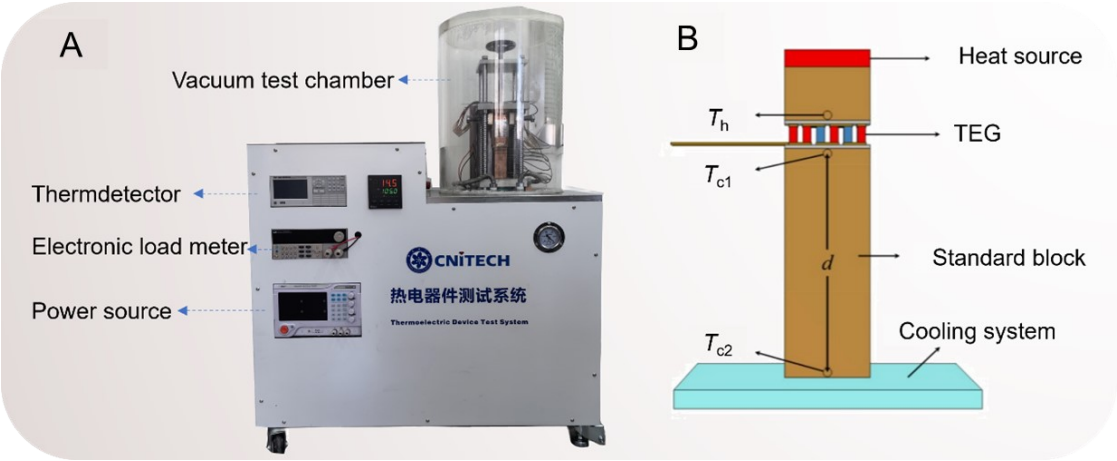

Fig. S31. (A) The testing system for thermoelectric conversion efficiency η measurement. (B) Schematic diagram of thermoelectric device test system.

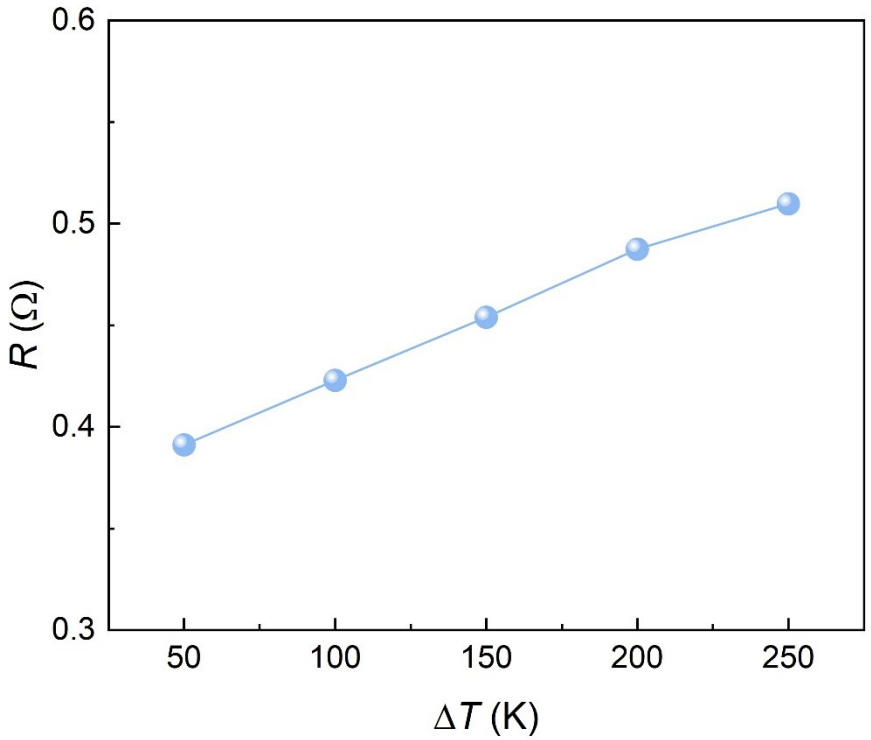

Fig. S32. The internal resistance (*R*) of the fabricated TE module at different gradient temperatures.

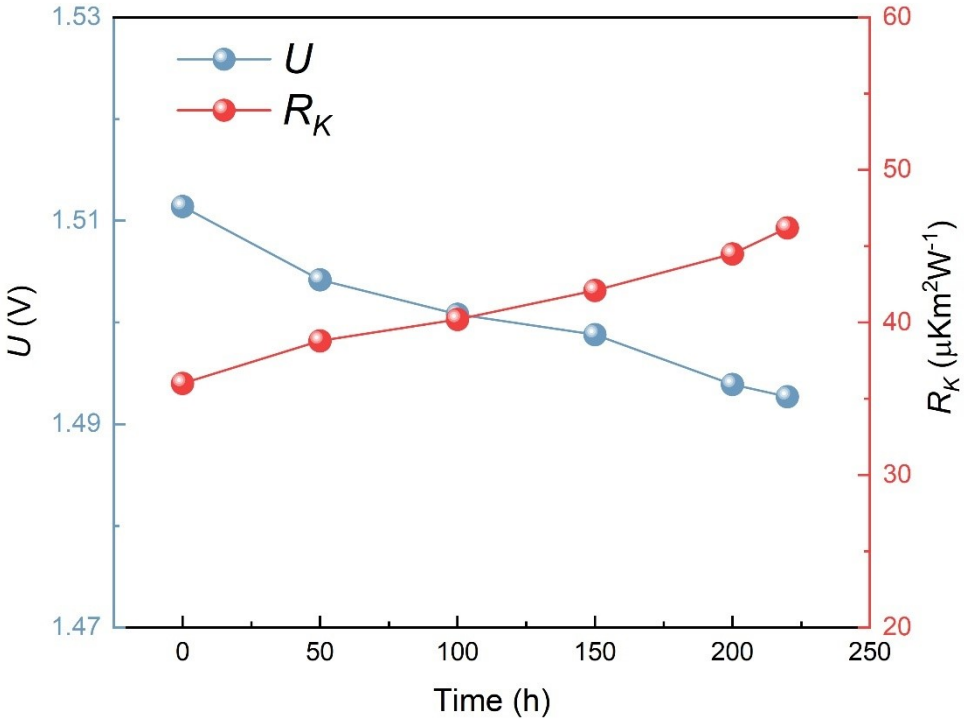

Fig. S33. Output voltage evolution during thermal cycling compared with simulated voltage levels corresponding to different thermal contact resistances.

Single Parabolic Band (SPB) model

Assuming a single parabolic band model and the dominant acoustic phonon scattering, [1-3] the Seebeck coefficient depends only on the reduced Fermi level η:

$$S = \pm\frac{k_B}{e}\left(\frac{F_1^2}{F_0^2} - \eta\right)$$

The hall concentration n_H and mobility μ_H can be calculated according to the following eqn.

$$n_H = \frac{16\pi\left(2m_d^* k_B T\right)^{1.5}}{3h^3}\frac{F_0^2}{F_{-0.5}}$$

$$\mu_H = \mu_0\frac{F_{-0.5}(\eta)}{2F_0(\eta)}$$

The electrical conductivity can be expressed as:

$$\sigma = \frac{8\pi e\left(2k_B T m_d^*\right)^{1.5}\mu_0}{3h^3}F_0 = \frac{8\pi e\left(2k_B T m_0\right)^{1.5}\mu_W}{3h^3}F_0$$

In the above equations, F_j is the Fermi integral:

$$F_j = \int_0^\infty \frac{x^j dx}{1 + e^{(x-\eta)}}$$

The calculation of *L* number

On the basis of the single parabolic band (SPB) model with acoustic phonon scattering dominating, the Lorenz number, L, can be derived from the following equations:[4]

$$L = \left(\frac{k_B}{e}\right)^2\left[\left(\frac{(\lambda+\frac{7}{2})F_{r+\frac{5}{2}}(\eta)}{(\lambda+\frac{3}{2})F_{r+\frac{1}{2}}(\eta)}\right) - \left(\frac{(\lambda+\frac{5}{2})F_{r+\frac{3}{2}}(\eta)}{(\lambda+\frac{3}{2})F_{r+\frac{1}{2}}(\eta)}\right)^2\right]$$

$$F_n(\eta) = \int_0^{\infty} \frac{x^n dx}{1 + e^{(x - \eta)}}$$

$$s = \pm \frac{k_B}{e} \left(\frac{(\lambda + \frac{5}{2}) F_{\lambda + \frac{3}{2}}(\eta)}{(\lambda + \frac{3}{2}) F_{\lambda + \frac{1}{2}}(\eta)} - \eta \right)$$

Where k_B is the Boltzmann constant, e is the electron charge, λ is the scattering parameter which equals to -0.5 for acoustic phonon scattering, $F_n(\eta)$ is the n-th order Fermi integral and η is the reduced Fermi energy.

The calculation of the lattice and bipolar thermal conductivity

When the bipolar effect is not taken into account at lower temperatures, the value of $\kappa_l + \kappa_b$ is approximately equal to the value of κ_l. The κ_l data between 300 K and 500 K can be obtained by fitting the relation $\kappa_l = aT^{-1} + b$, where a and b are the fitting parameters. Finally, the κ_b for all samples is obtained by subtracting the fitted κ_l and the calculated κ_e from the κ_{tot} measurement.

The calculation of average zT

Due to the intrinsic dependence of thermoelectric parameters on temperature, it is necessary to evaluate the thermoelectric properties of materials in a certain temperature range through average zT (zT_{avg}). The zT_{avg} can be calculated by the formula:

$$zT_{avg} = \frac{\int_{T_c}^{T_h} zT(T) dT}{T_h - T_c}$$

where T_h, T_c are the hot-side and cold-side temperatures.

Debye-Callaway model

The lattice thermal conductivity of $Bi_2Te_{2.79}Se_{0.21}$ + 0.12% BiI_3 and HD-803 are modeled by the Debye-Callaway model. In the Bi_2Te_3-based materials, acoustic

phonons are the major contributor to lattice thermal conductivity. [5]

$$\kappa_l = \frac{k_B}{2\pi^2 v}\left(\frac{k_B T}{\hbar}\right)\int_0^{\theta_a/T}\tau_{tot}(x)\frac{x^4 e^x}{(e^x-1)^2}dx$$

where $x = \hbar\omega/k_B T$ is the reduced phonon frequency, and v is the in-plane average speed of sound. τ is the total relaxation time and can be evaluated via the Matthiessen's rule,

$$\tau_{tot}^{-1} = \tau_U^{-1} + \tau_{PD}^{-1} + \tau_{GB}^{-1} + \tau_{DS}^{-1} + \tau_{NP}^{-1} + \tau_{NT}^{-1}.$$

The Umklapp phonon-phonon scattering (U),

$$\tau_U^{-1} = Ax^2T^3,$$

where A is the pre-factor of Umklapp scattering time, and it can be obtained by fitting in-plane transport parameters of the ZM sample.

The point defect phonon scattering (PD),

$$\tau_{PD}^{-1} = \frac{k_B^4 V_{PUC}}{4\pi\hbar^4 v^3}\Gamma x^4 T^4, \quad \Gamma = \sum_i f_i\left(\frac{M_i - \bar{M}}{\bar{M}}\right)^2,$$

where V_{PUC} is the volume of the primitive unit cell, Γ is the point defect scattering parameter and determined by the mass difference.

For common grain boundary, there is perfect acoustic mismatch at the interface between the material and vacuum, the relaxation times of phonons will be independent with the phonon frequency. The frequency-independent is given by

$$\tau_{GB}^{-1} = \frac{v}{d}$$

where v is the average sound velocity and d is the experimentally determined grain size.

The dislocations phonon scattering and concentrated stress phonon scattering (DS), [6, 7]

$$\tau_{DS}^{-1} = N_D \frac{\bar{V}^{\frac{4}{3}}}{v^2}\left(\frac{xk_BT}{\hbar}\right)^3 + 0.6B_D^2 N_D(\gamma + \Delta\gamma)^2 \frac{xk_BT}{\hbar}\left\{\frac{1}{2} + \frac{1}{24}\left(\frac{1-2r}{1-r}\right)^2\left[1 + \sqrt{2}\left(\frac{v_L}{v_T}\right)\right]^2\right\},$$

$$\Delta\gamma = \frac{V_{ST}C_0K}{k_B T_a}(\gamma\alpha^2 - \alpha\beta),\ \alpha = \frac{V_{BT} - V_{ST}}{V_{ST}},\ \beta = \frac{M_{ST} - M_{BT}}{2M_{ST}},$$

where N_D, B_D, γ, C_0, K, T_a and r is respectively the dislocation density, the effective Burger's vector, the Grüneisen parameter, the concentration of Bi_2Te_3 in $Bi_2Te_{2.79}Sb_{0.21}$, the bulk modulus of Bi_2Te_3, the sintering temperature and the Poisson's ratio. In addition, the parameters required for the Debye-Callaway model are summarized in Table S1.

Nano-sized Sb-rich precipitates are ubiquitous in both AGS and AGS/Cu samples. In the Debye-Callaway model, their effect is included as a Rayleigh-type nanoparticle-scattering term,

$\tau_{NP}^{-1} = A_{NP} f r^3 \omega^4$, where f is the volume fraction of nanoprecipitates, r is their average radius, and A_{NP} is a constant containing the elastic and mass-contrast factors. TEM statistics give r = 20 nm and a number density of ~3.3×10^{19} m^{-3} for both samples (Table S2), leading to a very similar fr^3 actor. As a result, nanoprecipitate scattering mainly provides a comparable high-frequency background in AGS and AGS/Cu and does not account for the additional reduction of κ_l in the nanotwinned sample.

Coherent nanotwins are only abundant in the AGS/Cu sample. They are treated as internal diffuse interfaces characterized by the twin-lamella spacing L_{NT}. The corresponding scattering rate is written as

$\tau_{NT}^{-1} = \frac{v}{L_{NT}}$, with $L_{NT} \approx 100$ nm determined from TEM measurements (Table S2). This term mainly scatters phonons whose intrinsic mean free paths are comparable to L_{NT}, i.e., mid-frequency modes in the 0.5-2 THz range at 300-500 K. Including τ_{NT}^{-1} in AGS/Cu significantly suppresses $\kappa_s(\omega)$ in this frequency window and allows the

calculated κ_l(T) to reproduce the experimentally observed extra κ_l reduction between 350 and 500 K.

The calculation of orientation factor *F*

The orientation factor *F*, denoting the degree of orientation in layered-structural samples, is determined through the Lottering method and is succinctly represented by the subsequent equation: [7]

$$F_{00l} = \frac{P - P_0}{1 - P_0}$$

$$P_0 = \frac{\Sigma I^0_{00l}}{\Sigma I^0_{hkl}}$$

$$P = \frac{\Sigma I_{00l}}{\Sigma I_{hkl}}$$

where I(00*l*) is the intensity of the diffraction peaks of (00*l*) planes, $\sum I_{hkl}$ is the total intensity of all (*hkl*) diffraction peaks and P is the ratio of the intensity of (00*l*) plane in the measured data. Similarly, I_0(00*l*), I_0(*hkl*), and P_0 denote the corresponding parts derived from the standard power diffraction file. The orientation factor *F* values, ranging from 0 to 1, signify the degree of sample orientation, with 0 indicating no preferred orientation and 1 denoting full orientation. The results of calculating the orientation factor F_{00l} for all samples are summarized in Fig. S3A.

Multi-physics field simulations

The multi-physics field simulations of conversion efficiency in this work were performed using the COMSOL program and the corresponding "Thermoelectric Effect" module. [8] A three-dimensional model of a 17-pair thermoelectric module with TE legs, Cu electrodes, insulating ceramic substrates, and a load is built. The temperature-dependent *S*, σ, and κ_{tot} of our *n*-type $Bi_2(Te,Se)_3$ and the *p*-type $(Bi,Sb)_2Te_3$

counterparts were collected as the input to the program. The thermoelectric effect in a steady state can be expressed by a set of differential equations with temperature (T) and electric potential (V) as two unknown variables. Electrical current density (J) and heat flux (q), as intermediate variables, are vectors in three spatial directions with a unit of A m^{-2} and W m^{-2}, respectively.

$$J = \sigma(-\nabla V - S\nabla T)$$

$$q = -k_{tot}\nabla T$$

$$\nabla J = 0$$

$$\nabla(k_{tot}\nabla T) + J^2/\sigma - TJ\nabla S = 0$$

where s denotes the electrical conductivity, equivalent to inversed resistivity[9-11].

The three-dimensional distribution of J, q, V, and T was numerically solved under given electrical and thermal boundary conditions. Important values which characterize the module such as electrical current I, terminal voltage $V(I)$, heat dissipated from the cold side of the module $Q_C(I)$, and electrical power output $P(I)$ were calculated from J, q, V and T. More precisely, $Q_C(I)$ was estimated by using either area integration of q over the bottom substrate of the module, and P was determined by volumetric integration of Joule heat J^2/σ inside the electrical load resistance in the model. Experimental control parameters such as hot- and cold-side temperatures T_h and T_c and electrical load resistance R_L were changed by a parametric sweep function of the software to simulate the real module testing. The efficiency η of the module was then determined using eqn $\eta = P/P + Q_c$ as a function of current I. Total time required for the simulation of current voltage curves at a certain temperature difference was several tens of seconds using a high-end personal computer. The theory efficiency of TE module could be given as following equations:

$$\eta_{max} = \frac{T_h - T_c \quad (1+\bar{z}T)^{1/2} - 1}{T_h \quad (1+\bar{z}T)^{1/2} + T_c/T_h}$$

$$\bar{z} = \left(\frac{\bar{S}_p + \bar{S}_n}{\sqrt{\kappa_p/\sigma_p}\sqrt{\kappa_n/\sigma_n}}\right)^2$$

$$\bar{S} = \frac{1}{T_h - T_c}\int_{T_c}^{T_h} S(T)dT$$

$$\bar{\sigma} = \frac{1}{T_h - T_c}\int_{T_c}^{T_h} \sigma(T)dT$$

$$\bar{\kappa} = \frac{1}{T_h - T_c}\int_{T_c}^{T_h} \kappa(T)dT$$

Table S1. Parameters for the lattice thermal conductivity of Bi_2Te_3-based materials in the Debye-Callaway model.

Parameters	Notes	Values
v	In-plane average speed of sound	1778 ms^{-1}
θ_D	Debye temperature	164 K
A	Prefactor of Umklapp scattering time	83400 $K^{-3}s^{-1}$
V_{PUC}	Volume of the primitive unit cell	$5\times\bar{V}$
$\bar{V}$	Average volume per atom	3.46×10^{-29} m^3
N_D	Dislocation density	1.8×10^{13} m^{-2}
B_D	Effective Burger's vector	3.9×10^{-9} m
γ	Grüneisen parameter	1.5

v_L	Longitudinal sound velocity	2800 m/s[3]
v_T	Transverse sound velocity	1600 m/s[3]
V_{BT}	Atomic volume of Bi_2Te_3	3.48×10^{-29} m^3
V_{ST}	Atomic volume of Sb_2Te_3	3.31×10^{-29} m^3
M_{BT}	Atomic mass of Bi_2Te_3	2.66×10^{-25} Kg
M_{ST}	Atomic mass of Sb_2Te_3	2.07×10^{-25} Kg
C_0	Concentration of Bi_2Te_3 in $Bi_{0.48}TeSb_{1.52}Te_3$	0.25
K	Bulk modulus of Bi_2Te_3	37.4 GPa
r	Poisson's ratio	0.14
$\Delta\gamma$	Changed Grüneisen parameter	1.47

Table S2. Microstructural parameters used in the Debye–Callaway analysis for the AGS and AGS/Cu samples.

	$Bi_{0.48}Sb_{1.52}Te_3$-AGS	$Bi_{0.48}Sb_{1.52}Te_3$-AGS/Cu
Grain size	0.67 μm	1.29 μm
Dislocation density	1.81×10^{14} m^{-2}	1.40×10^{14} m^{-2}
Average radius of nanoscale precursors	20 nm	20 nm
Number density of nanoscale precursors	3.3×10^{19} m^3	3.3×10^{19} m^3
Nanotwin size	/	100 nm

Reference:

[1] H. Wang, R. Gurunathan, C. Fu, R. Cui, T. Zhu and G. J. Snyder, *Materials Advances*, **2022**, 3, 734-755.

[2] N. Jia, J. Cao, X. Y. Tan, J. Dong, H. Liu, C. K. I. Tan, J. Xu, Q. Yan, X. J. Loh and A. Suwardi, *Materials Today Physics*, **2021**, 21.

[3] K. Pang, M. Yuan, Q. Zhang, Y. Li, Y. Zhang, W. Zhou, G. Wu, X. Tan, J. G. Noudem, C. Cui, H. Hu, J. Wu, P. Sun, G. Q. Liu and J. Jiang, *Small*, **2023**, DOI: 10.1002/smll.202306701, e2306701.

[4] B. Zhu, X. Liu, Q. Wang, Y. Qiu, Z. Shu, Z. Guo, Y. Tong, J. Cui, M. Gu and J. He, *Energy & Environmental Science*, **2020**, 13, 2106-2114.

[5] J. Callaway, *Physical Review*, **1959**, 113, 1046-1051.

[6] E. S. Toberer, A. Zevalkink and G. J. Snyder, *Journal of Materials Chemistry*, **2011**, 21, 15843.

[7] Z. Chen, X. Zhang, S. Lin, L. Chen and Y. Pei, *National Science Review*, **2018**, 5, 888-894.

[8] L. Yi, H. Xu, H. Yang, S. Huang, H. Yang, Y. Li, Q. Zhang, Z. Guo, H. Hu, P. Sun, X. Tan, G. Liu, K. Song and J. Jiang, *Journal of Power Sources*, **2023**, 559.

[9] B. Sherman, R. R. Heikes and R. W. Ure, Jr., *Journal of Applied Physics*, **2004**, 31, 1-16.

[10] X. Hu, H. Takazawa, K. Nagase, M. Ohta and A. Yamamoto, *Journal of Electronic Materials*, **2015**, 44, 3637-3645.

[11] X. Hu, P. Jood, M. Ohta, M. Kunii, K. Nagase, H. Nishiate, M. G. Kanatzidis and A. Yamamoto, *Energy & Environmental Science*, **2016**, 9, 517-529.